

# An Inquiry into Datacenter TCO for LLM Inference with FP8

Jiwoo Kim<sup>1\*</sup>, Joonhyung Lee<sup>2\*</sup>, Gunho Park<sup>2</sup>, Byeongwook Kim<sup>2</sup>, Se Jung Kwon<sup>2</sup>,  
Dongsoo Lee<sup>2</sup>, Youngjoo Lee<sup>3</sup>

<sup>1</sup>POSTECH, <sup>2</sup>NAVER Cloud, <sup>3</sup>KAIST

jiu.0210@postech.ac.kr, joonhyung.lee@navercorp.com, youngjoo@kaist.ac.kr

**Abstract**—As large language models (LLMs) continue to scale, the high power consumption of AI accelerators in datacenters presents significant challenges, substantially increasing the total cost of ownership (TCO) for cloud service providers (CSPs) that provide LLM inference. In this work, we analyze the computational characteristics of LLM inference from a TCO perspective and present a generalizable framework to compare AI accelerators across diverse operational requirements. Using this model, we investigate key workload characteristics influencing TCO for AI accelerators from Intel (Gaudi 2 & 3) and NVIDIA (H100 & H200), especially thin GEMM utilization and FP8 quantization. In particular, as FP8 emerges as the baseline precision for next-generation LLMs, understanding how different architectures implement and benefit from low-precision computation is increasingly critical. Throughput on thin GEMMs has a greater impact on TCO than theoretical hardware peak throughput because the memory-bound decode phase is dominated by GEMV-like computations. We find that Gaudi HPUs achieve superior utilization on thin GEMMs compared to their counterparts, especially in FP8-quantized models. Our result underscores the importance of empirical, workload-level analysis in evaluating accelerator performance, rather than relying solely on theoretical hardware specifications. By studying the interaction between power consumption, quantization strategies, and hardware architecture, we provide insights to support informed deployment decisions and guide future accelerator designs aimed at improving the TCO of LLM inference workloads.

## I. INTRODUCTION

The rapid advance of large language models (LLMs) has made AI datacenters essential infrastructure for timely and reliable inference workloads. As ever more users submit longer and more complex requests, the number of generated tokens has risen sharply. The financial and energy burden of deploying LLMs at scale has reached the point where hyperscalers are planning colossal datacenters that would require multiple nuclear power plants to operate. For instance, a single phase of the Stargate project plans to add 4.5 GW of datacenter capacity [1, 2], while Meta has separately announced plans for a 2 GW datacenter [3]. To put these figures into perspective, a typical nuclear power plant generates approximately 1 GW [4] and New York City had a peak electricity consumption of 10.8 GW in 2024 [5].

Among the various workloads in the AI pipeline, LLM inference exhibits unique characteristics that require specialized analysis. Unlike highly regular training workloads, LLM inference, particularly the decoding phase, is dominated by memory access and is highly latency sensitive. With the increasing

popularity of “reasoning” AI models for both proprietary models, such as ChatGPT o1 [6] and Claude 3.7 [7], as well as open-weight models such as DeepSeek R1 [8] and Qwen3 [9], the number of output tokens per query has significantly increased. As a result, the decoding phase has become the primary performance bottleneck, often dominating prefill in both execution time and system resource usage. This decode-heavy behavior is particularly challenging because it stresses memory bandwidth rather than compute throughput, which many accelerators have traditionally been optimized for.

Despite ongoing advances in AI accelerator design [10, 11] and quantization techniques for LLMs [12, 13, 14], relatively little attention has been paid to how these innovations affect the total cost of ownership (TCO) at datacenter scale. Moreover, while previous studies [15, 16] have analyzed throughput-cost trade-offs, they are often limited to specific deployment scenarios. In this work, we address this gap by developing a holistic TCO model for LLM inference that accommodates a wide range of cost structures and performance requirements, allowing for flexible evaluation across various cloud service provider (CSP) contexts. Our goal is to provide practical guidance for CSPs by enabling comparisons between hardware options that consider both facility costs and target performance levels. In this work, we present a generalizable TCO estimation framework for selecting AI accelerators in datacenters that emphasizes (1) hardware characteristics related to the numerical precision and (2) workload characteristics specific to the LLM inference.

One of the most effective levers for improving both computational efficiency and memory bandwidth in LLM inference is lowering numerical precision. For next-generation LLMs, FP8 is emerging as a de facto baseline data precision. Recent AI accelerators have begun to incorporate dedicated hardware units optimized for FP8 general matrix-matrix multiplication (GEMM), prompting major model providers to adopt FP8 quantization in production-scale models such as DeepSeek-V3 [17] and Qwen3 [9]. While improvements in dense BrainFloat16 (BF16) [18] GEMM throughput and memory bandwidth continue in recent GPU generations, gains in energy efficiency are plateauing, as we show in Table I. Our analysis suggests that focusing solely on high-performance hardware can lead to suboptimal datacenter management, highlighting the necessity of adopting software optimizations, especially low-precision computation.

While FP8 provides a promising path toward improved inference efficiency, fully leveraging its potential requires a deeper understanding of workload-specific bottlenecks in LLM inference and corresponding architectural support. The computational characteristics of LLM inference differ considerably from those of training. Even within the inference process, the prefill and decode phases have distinct workloads. While the prefill phase is similar to the forward pass of training, the decode phase is dominated by thin GEMM operations, which are also referred to as skinny GEMMs, that resemble Generalized Matrix-Vector (GEMV) computations. Thin GEMMs exhibit low computational intensity (CI) and lead to reduced model FLOP utilization (MFU) [19, 20]. Unlike most prior works, we perform roofline analysis separately for each phase of LLM inference rather than measuring only the output token throughput across different input/output sequence length configurations. TFLOPS values are calculated for disaggregated workloads instead of TTFT and TPOT [15] in mixed workloads, enabling precise comparisons of computational efficiency relative to the peak throughput at various configurations.

To summarize our contributions:

- 1) We provide a simple framework for comparing the relative cost and throughput for different AI accelerators. Although an oversimplification of the true complexities involved, we believe that our model is general enough for end users to find the balance that suits them best by substituting their actual costs and constraints into the variables we define.
- 2) Despite the growing popularity of FP8 quantization as a method that offers favorable trade-offs between throughput and memory efficiency, prior work has largely overlooked its empirical evaluation, particularly in the context of hardware-specific behavior during LLM inference. To address this gap, we measure FP8 performance across accelerators from Intel (Gaudi 2 & 3) and NVIDIA (H100 & H200).
- 3) Finally, we provide a focused investigation of LLM decoding throughput that goes beyond a simple inspection of hardware specifications. By examining the performance characteristics and bottlenecks of each device within LLM workloads under FP8-quantized conditions, we offer insights that inform both hardware design and deployment strategies.

## II. EXPLORING THE TCO-THROUGHPUT TRADE-OFF

### A. Understanding the TCO Model

When calculating the costs involved in running AI accelerators for datacenter operators, the purchase price of the chips, while significant, constitutes only part of the TCO [21]. For example, the purchase cost of the networking, cooling, and power infrastructure necessary to maintain the processors is frequently as large as the purchase cost of the chips and may even exceed it [22]. As AI inference workloads constitute an ever greater portion of datacenter operations, achieving low cost and high efficiency requires careful planning. The

TCO Ratio (A / B)		Server Cost Ratio ( $R_{SC}$ )									
		1.00	0.90	0.80	0.70	0.60	0.50	0.40	0.30	0.20	0.10
Throughput Ratio ( $R_{Th}$ )	1.00	1.00	0.95	0.90	0.85	0.80	0.75	0.70	0.65	0.60	0.55
	0.90	1.11	1.06	1.00	0.94	0.89	0.83	0.78	0.72	0.67	0.61
	0.80	1.25	1.19	1.13	1.06	1.00	0.94	0.88	0.81	0.75	0.69
	0.70	1.43	1.36	1.29	1.21	1.14	1.07	1.00	0.93	0.86	0.79
	0.60	1.67	1.58	1.50	1.42	1.33	1.25	1.17	1.08	1.00	0.92
	0.50	2.00	1.90	1.80	1.70	1.60	1.50	1.40	1.30	1.20	1.10
	0.40	2.50	2.38	2.25	2.13	2.00	1.88	1.75	1.63	1.50	1.38
	0.30	3.33	3.17	3.00	2.83	2.67	2.50	2.33	2.17	2.00	1.83

Fig. 1. TCO comparison table for fixed traffic. For any desired task, given the throughput ratio between accelerators A and B  $R_{Th}$  and server price ratio  $R_{SC}$ , the table shows the TCO of accelerator A as a proportion of the TCO of accelerator B. Accelerator A is therefore more cost-efficient than B when the obtained value is less than 1. The lower the value, the greater the cost-effectiveness of A. The values in Equation 4 are calculated by assuming  $Cost_{Server,B} = Cost_{Infra,B} = Cost_{Infra,A}$ .

choice of accelerator impacts both the throughput and the power consumption, both of which have a substantial influence on TCO. At large scales, performance per dollar is the most critical metric [21]. However, because costs continue to change and often cannot be revealed, we provide a generalizable model where CSPs can enter their own costs and evaluate the results.

Consider a scenario in which a CSP chooses accelerators for a datacenter. Two alternatives exist: accelerator A, which is lighter-weight, delivers lower peak specifications, and has a lower purchase price, and accelerator B, which provides substantially higher peak specifications but comes with a higher per-accelerator purchase price. To identify which option yields higher profitability, a model to compare TCO values between the two accelerators is needed. A server contains not only the chip, but also networking, storage, and other associated components. Multiple chips may also be located in a single server. In the following discussion, we denote  $Cost_{Server}$ , abbreviated as  $Cost_{Sv}$ , as the combined purchase costs of the multiple accelerator chips, CPUs, storage, and networking devices required to constitute an operational server.

To clarify the analysis, we use  $Cost_{Infra}$ , abbreviated as  $Cost_{If}$ , to indicate the infrastructure costs associated with operating the datacenter, including cooling and power provision, divided by the number of servers. Operating expenses (OpEx) such as electricity consumption are also included in  $Cost_{Infra}$ . To understand the infrastructure cost, note that while the cost of electricity consumption increases almost linearly with regard to the number of processors, the cost of the associated infrastructure, such as power racks and cooling equipment, is nearly constant. Because datacenter racks can only provide a limited amount of power, the per-chip cost of infrastructure is inversely proportional to the number of servers

that fit in a single rack, which in turn depends on the power consumption of the server. Therefore, the benefits of lower power consumption are twofold: the electricity consumption goes down, and the number of processors per rack increases, spreading fixed infrastructure costs among a greater number of servers. For most datacenters, the cost of electricity is outweighed by the cost of the rack and cooling equipment, even when amortized over several years, leading  $Cost_{Infra}$  to be most heavily affected by the number of chips per rack. We denote  $R_{Th}$  as the throughput ratio between a single server of accelerators A and B. We also denote  $R_{SC}$  as the cost ratio between accelerators A and B. They are defined as follows:

$$R_{Th} = \frac{Throughput_A}{Throughput_B} \quad (1)$$

$$R_{SC} = \frac{Cost_{Server,A}}{Cost_{Server,B}} \quad (2)$$

$$R_{IC} = \frac{Cost_{Infra,A}}{Cost_{Infra,B}} \quad (3)$$

Regardless of the devices in use, the amount of traffic remains constant. We therefore make an *iso-traffic* assumption and use  $N$  to represent the number of B servers required to process the expected traffic.

Assuming that the cost of infrastructure is the same for accelerators A and B, we derive the following equation:

$$\frac{TCO_A}{TCO_B} = \frac{Cost_{sv,B} \times R_{SC} \times \frac{N}{R_{Th}} + Cost_{If,B} \times R_{IC} \times \frac{N}{R_{Th}}}{Cost_{sv,B} \times N + Cost_{If,B} \times N} \quad (4)$$

The numerator captures the TCO incurred when scaling up the deployment of lower-performance accelerator A to meet the same throughput target as accelerator B. The denominator reflects the baseline TCO of using accelerator B for a given amount of traffic. As total traffic remains constant regardless of the underlying device, purchasing accelerator A will require  $R_{Th}/N$  nodes, leading to possibly increased infrastructure costs depending on the throughput ratio  $R_{Th}$ . At the same time, its lower per-chip cost, reflected in the server price ratio  $R_{SC}$ , could result in a lower TCO.

Based on this model, Figure 1 illustrates the TCO comparison between two accelerators, expressed as an  $A/B$  ratio. The x-axis represents the server price ratio, and the y-axis represents the per-server throughput ratio of the two accelerators for the desired task. Since exact costs are often confidential in real-world data centers [21], allowing users to plug in their costs and flexibly adapt to various operational contexts. The values in Figure 1 are an example of the TCO ratio between two hardware options. The lower the value, the less expensive (and hence more cost-effective) lighter-weight accelerator A becomes, and the more appealing it is to adopt. Conversely, a ratio above 1.0 suggests that higher-weight accelerator B is preferable from a TCO perspective.

### B. Visualizing the TCO Model

The TCO table provides interpretability for real-world datacenter environments that serve diverse applications. Figure 2

illustrates how the TCO ratio changes under varying conditions, with a focus on two key parameters: the throughput ratio ( $R_{Th}$ ) and the server cost ratio ( $R_{SC}$ ). Each coordinate in the table represents an evaluation point, where the color indicates the relative cost-efficiency between two accelerators.

Movement along the x-axis reflects the server cost ratio, which is influenced by device procurement costs, infrastructure constraints, and other datacenter-specific factors. Purchasing accelerator A at a discount would move the TCO ratio along the x-axis to the right. However, even accelerator A was given for free,  $Cost_{Server,A}$  and  $Cost_{Infra,A}$  would both be greater than 0, requiring careful inspection of  $R_{Th}$ .

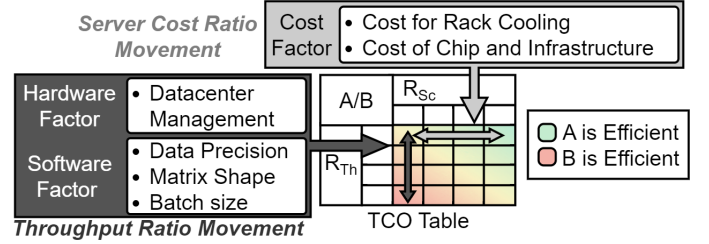


Fig. 2. Visualization of TCO Variation by Server Cost and Throughput Ratios.

The y-axis position, which reflects the throughput ratio  $R_{Th}$ , is highly dependent on two operational factors: (1) hardware characteristics related to the data precision and (2) workload characteristics.

As different models and stages of inference have different throughput values on different devices, there is no single throughput value, but many throughput values for each task. For example, increasing the batch size can improve the throughput of a device but comes at the cost of higher latency. The throughput of the accelerator could be defined as the throughput at the largest batch size that meets a specific latency requirement. Likewise, we could also use quantization to shift  $R_{Th}$ , possibly with the condition that only quantized models that pass specific quality controls may be considered. Accelerators can have different  $R_{Th}$  values for different inference phases, e.g., prefill and decode. The next sections discuss these topics in greater detail.

## III. FP8 FOR HIGH-THROUGHPUT LLM INFERENCE

TABLE I  
COMPARISON OF TECHNICAL SPECIFICATIONS ACROSS NVIDIA GPUS

	TFLOPS	TDP	TFLOPS/Watt	Increase
<b>V100 (SXM)</b>	125	300	0.42	-
<b>A100 (SXM)</b>	312	400	0.78	87%
<b>H200 (HGX)</b>	989	700	1.41	81%
<b>B300 (HGX)</b>	2,250	1,200	1.88	33%

### A. Motivation for FP8 Quantization

With the increasing adoption of FP8 GEMM in recent accelerator designs, the format is expected to become a next-generation standard for LLM inference. While most recent

LLMs continue to operate in BF16 precision, lowering precision offers a significant opportunity to boost throughput and reduce the TCO, as long as the accuracy degradation remains within acceptable limits. Despite these benefits, real-world deployment of low-precision inference remains challenging in practice. This is particularly true for decoder-only models, even when dynamic quantization is applied to activations. However, a new wave of foundation models such as DeepSeek-V3 and LLaMA 4 has demonstrated the feasibility of FP8 at scale. These models are trained using dynamic fine-grained FP8 quantization, showing that FP8 is a practical alternative to BF16 for achieving high-throughput inference while maintaining the quality of outputs.

Employing FP8 can often yield greater gains for LLM inference than simply adopting newer accelerators with improved memory bandwidth or peak compute performance. Table I compares key architectural specifications across four generations of NVIDIA GPUs: V100 [23], A100 [24], H200 [25, 26], and the upcoming B300 [27]. The comparison includes peak dense BF16 (except for the V100, which uses FP16) GEMM throughput in TFLOPS (TFLOPs per second), thermal design power (TDP), and energy efficiency measured in TFLOPS per Watt. Even relying solely on official specifications, the improvement in dense BF16 TFLOPS per Watt shows diminishing returns. The gains from V100 to A100 are significant, but the improvement from H200 to B300 is noticeably smaller. This suggests that simply scaling hardware resources is no longer sufficient to keep pace with the growing demand for LLM inference. The bottleneck increasingly lies in thermal and power constraints, which are exacerbated as more compute and I/O components are packed into limited physical space. As a result, software and algorithmic optimizations, particularly those involving low-precision formats such as FP8, are essential for the next generation of LLM infrastructure.

However, the effectiveness of low-precision computation depends heavily on the underlying hardware architecture. Although FP8 may offer up to twice the theoretical throughput compared to BF16, achieving this level of performance in practice is often difficult due to reduced hardware utilization. As the numerical precision decreases, it becomes harder for the system to keep all units busy, and performance bottlenecks in memory bandwidth, special function units (SFUs, also referred to as multi-function units, or MUFUs), or scheduling pipelines can prevent ideal throughput. Therefore, the actual benefits of FP8 are closely tied to the ability of the architecture to support low-precision computation efficiently. To guide future LLM deployment strategies, it is essential to perform TCO analysis that explicitly incorporates FP8-related considerations. Only by aligning hardware and software design around low-precision computation can datacenter architects fully realize the potential efficiency gains of FP8.

### B. Differences in Hardware Capabilities

Although FP8 is widely regarded as a numerical format, it is more accurately described as a form of quantization rather than a fully standardized datatype such as BF16 [18]. The

TABLE II  
COMPARISON BETWEEN DIFFERENT FP8 OPTIONS

Model	Data Type	Rounding	MMLU
Llama v3.2 1B Instruct	BF16	-	46.3%
	E4M3	SR	45.7%
	E4M3	RTN	45.5%
	E5M2	RTN	44.5%
Llama v3.2 3B Instruct	BF16	-	61.8%
	E4M3	SR	61.7%
	E4M3	RTN	61.6%
	E5M2	RTN	60.7%
Llama v3.1 8B Instruct	BF16	-	68.8%
	E4M3	SR	68.3%
	E4M3	RTN	68.3%
	E5M2	RTN	67.5%
Llama v3.3 70B Instruct	BF16	-	82.0%
	E4M3	SR	82.0%
	E4M3	RTN	82.0%
	E5M2	RTN	82.2%

behavior of FP8 depends strongly on the choice of scaling factor, which can vary in granularity from per-tensor to per-channel or even group-based approaches as in the MXFP8 [28] format. To explore these differences, we compare FP8 GEMM implementations on NVIDIA GPUs and Intel Gaudi HPUs, identifying key distinctions that affect both throughput and model accuracy despite all these devices conforming to the FP8 specification [10].

**(Binary formats)** Both NVIDIA GPUs and Intel Gaudi HPUs support the E4M3 and E5M2 formats [10]. E4M3 assigns one sign bit, four exponent bits, and three mantissa bits. E5M2 also assigns one sign bit but uses five exponent bits and only two mantissa bits. Previous works proposed using E4M3 for the forward pass, which is more sensitive to precision, and E5M2 for the backward pass, which is more sensitive to outliers. However, DeepSeek-V3 used E4M3 in both the forward and backward passes, showing that a smaller group size for scaling factors can compensate for the smaller value range of E4M3. Alternatives such as E3M4 have also been proposed [29], but have yet to be implemented in commercial hardware.

**(Accumulation precision)** Hopper GPUs use a 14-bit accumulator for FP8 GEMMs [17], requiring casting to CUDA cores for higher precision. Software optimizations, such as applying FP32 accumulation to only one in four warp-group matrix multiply-accumulate (WGMMMA) instructions, reduce error but increase kernel complexity and remain less precise than full FP32 accumulation. In contrast, Gaudi HPUs always accumulate in FP32 [11], ensuring higher numerical precision.

**(E4M3 range)** The Gaudi 2 follows the IEEE specification for special values, unlike NVIDIA GPUs and the Gaudi 3, which use a single special value representation [30]. This results in seven fewer magnitude representations and a maximum value of 240 for E4M3 in the Gaudi 2, compared to 448 on NVIDIA GPUs. This has been addressed in the Gaudi 3, which uses the same E4M3 format as NVIDIA GPUs. Note

that E5M2 follows the IEEE 754 specification for all devices.

**(Power-of-2 scaling)** Gaudi HPUs allow the modification of floating-point exponent biases to accelerate scaling factor application. The Gaudi 2 supports fixed hardware-accelerated scaling factors of  $2^{-8}, 2^{-4}, 2^0, 2^4$  for E4M3, while the Gaudi 3 extends this to arbitrary powers of 2 between  $2^{-32}$  and  $2^{31}$ . However, this feature is limited to per-tensor scaling factors.

**(Stochastic rounding)** During FP8 quantization, stochastic rounding can be applied when converting 16/32-bit floating-point values to FP8, similar to the technique proposed for FP32-to-BF16 conversion in [31]. This method is distinct from stochastic rounding applied at the inner-product [32]. However, we find that stochastic rounding does not meaningfully benefit output quality, as shown in Table II.

**(Sparsity)** NVIDIA GPUs support semi-structured sparsity acceleration, potentially doubling tensor core peak throughput. However, despite attempts to leverage semi-structured sparsity in LLM inference [33, 34], dense GEMMs remain dominant due to accuracy loss and limited speedups. Gaudi HPUs do not support semi-structured sparsity acceleration.

**(Quantization granularity)** Both Hopper GPUs and Gaudi 2&3 support standard FP8 [10], which has limited support for fine-grained quantization. However, starting with Blackwell [27], NVIDIA GPUs have adopted the MXFP8 [28] format, which uses an 8-bit power-of-2 shared scaling factor and a group size of 32.

#### C. Dynamic vs. Static: A Key FP8 Quantization Choice

A key consideration in utilizing FP8 is the activation quantization strategy. Weights are always quantized ahead of time, but activations must be quantized online before each GEMM operation. Commercially available AI accelerators require that both input matrices for GEMM operations be in FP8. However, operations such as SwiGLU or residual addition require the inputs to be in 16-bit, and RoPE [35] requires 32-bit [36]. Therefore, when multiplying activations with weights in an LLM, the activations are usually in BF16 and must be quantized online to FP8. During the online quantization of the activations, the quantization scaling factors can be obtained either statically or dynamically: calculated beforehand based on calibration data or dynamically during inference time [14, 37].

Static scaling factors have the advantage that they do not require an additional pass over the high-precision activation to obtain quantization statistics, e.g., the maximum absolute value of a tensor. However, it has the disadvantage that input activations may have a different distribution from the calibration set, causing performance degradation. LLMs often have outlier values in their activations [38], making it challenging to find static scaling factors that perform well for all inputs. Also, per-token fine-grained activation quantization is only possible for dynamic scaling factor quantization. Because inference batches consist of unrelated sequences, information to distinguish between different tokens in a batch is only available at runtime. Static scaling factors cannot apply different scaling factors to different tokens. In practice, this limits static

scaling to per-tensor quantization of the activations. Although various techniques, such as smoothing [14] and rotation-based methods [13, 39], can help mitigate output quality degradation, they rely on calibration data and may yield suboptimal scaling factors for unseen inputs. Dynamic scaling enhances output quality by assigning separate scaling factors to each token. As a result, dynamic quantization remains the preferred approach, and native FP8 foundation models such as DeepSeek-V3 and Llama 4 use dynamic activation scaling factors for both training and inference. This restriction does not apply to the weights, which can apply fine-grained static scaling factors during offline quantization. For example, DeepSeek-V3 and Qwen3 use a group size of  $128 \times 128$  for their FP8 weights.

#### D. Comparison Between FP8 Options

We analyze the impact of applying the E4M3 and E5M2 formats, as well as stochastic rounding (SR), on instruction-tuned LLMs in Table II. All evaluations were conducted on an Intel Gaudi 2 HPU using instruction-tuned LLaMA models with dynamic FP8 scaling factors. Performance was measured on the MMLU benchmark with 5-shot chain-of-thought (CoT). Our results show that E4M3 consistently outperforms E5M2, which is in line with previous work [29].

Stochastic rounding might be expected to preserve more numerical information during quantization by introducing randomness that avoids systematic rounding bias, which could help maintain model accuracy. However, our experiments in Table II indicate that applying stochastic rounding during FP8 quantization does not lead to meaningful accuracy improvements. In some cases, it even slightly reduces accuracy, consistent with observations from prior work [31]. These findings suggest that the practical value of stochastic rounding for FP8 inference for instruction-tuned LLMs remains limited.

### IV. PHASE-AWARE ANALYSIS OF FP8 LLM INFERENCE

#### A. LLM Inference Phases

Generative LLM inference comprises two distinct phases: a compute-bound prefill phase and a memory-bound decode phase [15, 40]. Figure 3 illustrates the key differences between these phases. During the prefill phase, the LLM generates the first output token based on the input prompt. The key-value (KV) pairs generated during prefill are stored in the KV cache for reuse in subsequent token generation. The prefill phase processes the entire input in parallel, utilizing large compute-bound GEMMs. This high degree of parallelism enables efficient input processing.

After the first token is generated, the process transitions into the decode phase, where the model generates tokens autoregressively one at a time, conditioning each output on all previously generated tokens. Unlike the prefill phase, the decode phase is constrained by memory capacity and bandwidth because it involves GEMV and thin GEMM operations, inherently limiting hardware utilization. Inference frameworks such as vLLM [41] and TensorRT-LLM [42] mitigate this issue by batching multiple decoding requests together. This increases the computational intensity (CI) of the linear layers,



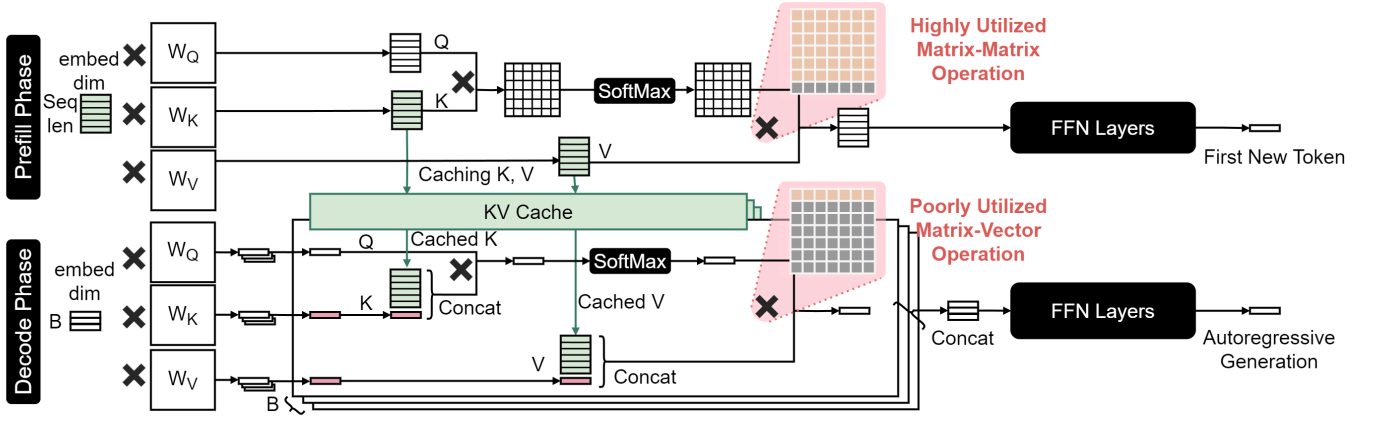


Fig. 3. Process and utilization characterization of the two phases of generative LLM inference. The prefill phase processes multiple tokens from the same sequence simultaneously, allowing efficient compute-bound computation that produces a single KV cache. The decode stage batches many sequences to improve the computational intensity at the linear layers, but is limited by memory because each sequence has a separate KV cache.

improving throughput. However, batching is fundamentally limited by memory capacity because each sequence in the batch requires its own KV cache. Moreover, the attention operation during decoding does not benefit from increased batch size. Each sequence still requires a separate GEMV for attention, which prevents CI improvements. This bottleneck becomes more noticeable at longer sequence lengths. While the number of FLOPs required for linear layers remains constant, the FLOPs for attention increase linearly with sequence length. Grouped Query Attention (GQA) [43] reduces the overhead by converting the attention computation into a thin GEMM. Although this increases efficiency, the operation remains memory-bound. Multi-head Latent Attention (MLA) [44] further improves the computational intensity of the decode phase, yet the fundamental limitation persists.

### B. Calculating GEMM FLOPs

For a GEMM between matrices of size  $(M \times K) \times (K \times N)$ , the total number of floating-point operations (FLOPs) performed is  $2MK N$ . This is derived from the  $M \times N$  dot products of length  $K$ , where each element undergoes one multiplication and one addition.  $M$  corresponds to typical batch sizes during inference and  $K, N$  represent hidden dimension sizes. Following the convention where FLOPS denotes FLOPs per second, we compute throughput in FLOPS using the theoretical FLOPs and the measured latency. The model FLOPs utilization (MFU) [19] is derived by dividing the observed throughput by the hardware specification throughput.

### C. Calculating Inference FLOPs

While previous works [15] have evaluated inference performance using time to first token (TTFT) and time per output token (TPOT), these metrics do not facilitate comparisons across different inference stages, model sizes, or sequence lengths. To ensure a consistent comparison, we directly compute model FLOPs. We follow the methodology described in [20, 45], computing only the FLOPs associated with matrix multiplications and excluding those related to autoregressive

attention masking, which can be skipped [46]. This yields a more faithful representation of the actual decoding FLOPs.

Using this method, the FLOPs required for a forward pass of a Llama model with  $l$  transformer blocks, hidden size  $h$ , intermediate size  $ah$ , head size  $d$ , head count  $H = h/d$ , GQA group size  $g$ , vocabulary size  $v$ , and input sequence of length  $s$  can be calculated as follows:

$$f_{llama}(s) = 2sh^2l(3a + 2 + \frac{2}{g}) + 2s^2hl + 2vsh. \quad (5)$$

By denoting  $A = (3a + 2 + \frac{2}{g})$  as a model-specific constant, Equation 5 simplifies to:

$$f_{llama}(s) = 2s(Ah^2l + vh) + 2s^2hl. \quad (6)$$

When the model generates  $t$  tokens in a single decoding iteration where  $t \ll s$ , we approximate the additional computation by evaluating Equation 5 at  $s' = s + t$ , yielding:

$$\begin{aligned} f_{llama}(s+t) - f_{llama}(s) \\ \approx 2t(Ah^2l + vh) + 4sth. \end{aligned} \quad (7)$$

From Equation 7, we observe that the computational cost of the linear layers, including the LM head, remains independent of the previous sequence length  $s$ , while the attention-related FLOPs scale proportionally with  $s$ . In the autoregressive setting where  $t = 1$ , and for a batch of  $b$  sequences with respective sequence lengths  $s_1, \dots, s_b$ , the FLOPs required for one decoding step can be approximated as:

$$2b(Ah^2l + vh) + 4hl \sum_{i=1}^b s_i. \quad (8)$$

A key observation is that only the  $2bAh^2l$  term, corresponding to the linear layers (excluding the LM head), is computed in FP8. In contrast, the  $2bvh$  term for the LM head and the  $4hl \sum_{i=1}^b s_i$  term for attention are computed in BF16. Additionally, online dequantization of the KV cache introduces extra overhead not accounted for in Equation 8 as these overheads do not contribute to the model FLOPs as defined in the MFU metric [19].

#### D. Challenges in Achieving Peak Throughput

A fundamental limitation in LLM inference is that not every FLOP can be executed at peak efficiency, primarily due to hardware utilization constraints. For instance, the Gaudi 2 provides a peak HBM bandwidth of 2.4 TB/s and a peak FP8 GEMM throughput of 865 TFLOPS. This implies that a computational intensity (CI) of at least 360 FLOPs/byte is required to saturate the compute units. However, during the decoding phase, the workload often reduces to a thin GEMM with shape  $(b \times h) \times (h \times ah)$ , where  $b \ll h$  and  $a \geq 1$ . In such cases, the resulting CI drops to approximately  $2b$  for FP8 and  $b$  for BF16, which is much lower than the threshold needed to achieve peak throughput at realistic batch sizes. Furthermore, matrix multiplication units are typically optimized for fixed-size tile shapes, and high hardware utilization is only attainable when input dimensions align with hardware-friendly boundaries, such as multiples of 128 [47].

KV cache computations are another bottleneck. Unlike linear layers, increasing the batch size does not improve CI in attention because each sequence in the batch maintains a separate KV cache. For example, in a BF16 KV cache with grouped query attention (GQA) using  $g$  groups, the CI is bounded by  $g$  FLOPs per byte. As a result, even in an ideal implementation, the maximum achievable throughput for querying the KV cache is limited by the product of memory bandwidth and CI. In the case of an LLaMA v3.1 8B Instruct model with  $g = 4$  running on a Gaudi 2, this translates to a theoretical upper bound of  $2.4\text{TB/s} \times 4 = 9.6$  TFLOPS. Because attention computations are inherently memory-bound and the number of FLOPs required for them scales linearly with sequence length, decoding becomes increasingly constrained by attention throughput as sequence lengths grow. Recognizing the distinct compute characteristics of each phase enables more effective optimization strategies, particularly in improving decode phase efficiency, which often dominates end-to-end inference latency.

### V. EMPIRICAL COMPARISONS

#### A. Prefill Phase

Figure 4 presents a comparison of prefill throughput, measured in TFLOPS, for the LLaMA v3.1 8B Instruct model across various input sequence lengths on the Gaudi 2, Gaudi 3, H100, and H200 for BF16, static FP8 scaling, and dynamic FP8 scaling. The results show that prefill performance is primarily determined by GEMM throughput rather than memory bandwidth. The H100 and H200 GPUs show a higher prefill throughput than the Gaudi 2, in line with their higher specifications. The Gaudi 3 has a lower throughput than the H200, despite having a peak BF16 GEMM throughput of 1678 TFLOPS [48] compared to 989.4 TFLOPS for the H200 [26]. We explore the reasons for this discrepancy in Section VI.

All accelerators exhibit higher throughput when using FP8 compared to BF16. For NVIDIA GPUs, static scaling yields slightly better performance than dynamic scaling, as dynamic scaling incurs an overhead of computing scaling factors during

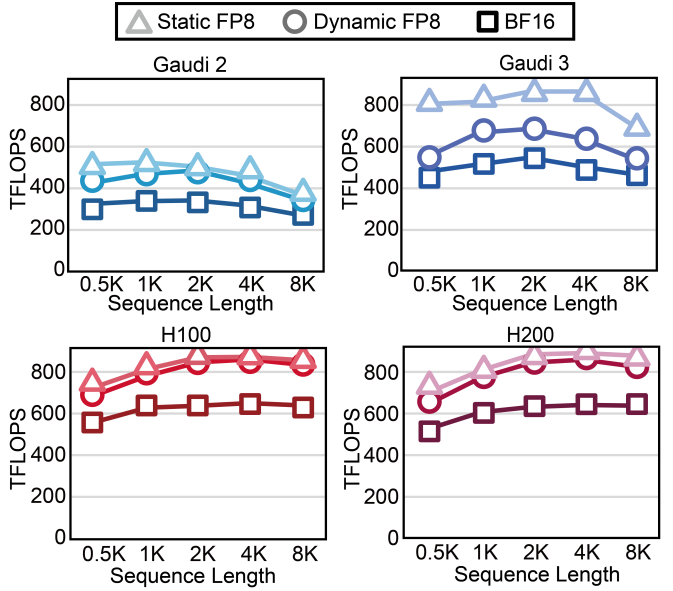


Fig. 4. Diagram showing prefill phase throughput measurements for batch size 1. Throughput improves with longer sequence lengths until they begin to decline as the proportion of attention computations, which are slower than GEMMs, takes up a greater share of the computation.

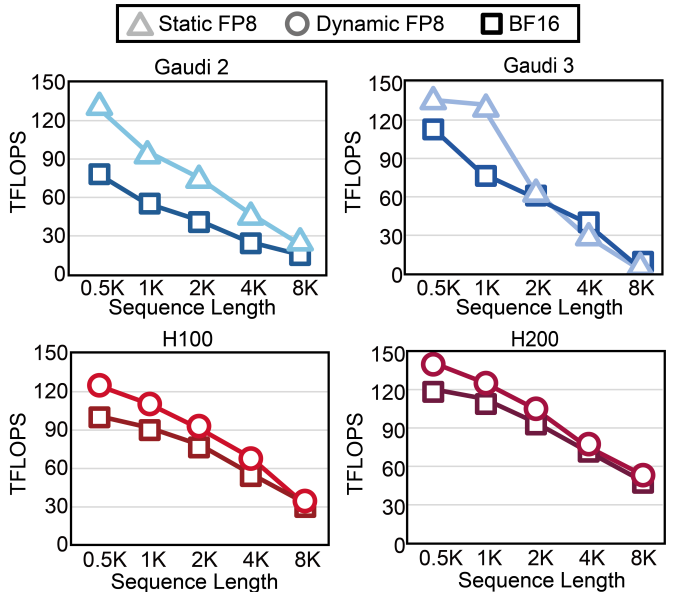


Fig. 5. Decode throughput comparison between BF16 and FP8 on Llama v3.1 8B Instruct using a batch size of 64 using static FP8 scaling on the Intel HPU (Gaudi 2 & 3, top) and dynamic FP8 scaling on NVIDIA GPUs (H100 & H200, bottom). Throughput differences between FP8 and BF16 in the Gaudi 2 are 50% or greater, whereas they are under 25% for the H100 and H200.

inference time. The performance gap for Gaudi devices between static and dynamic scaling is larger, which we attribute to the immaturity of the dynamic scaling implementation, which was not feature-complete as of the time of writing.

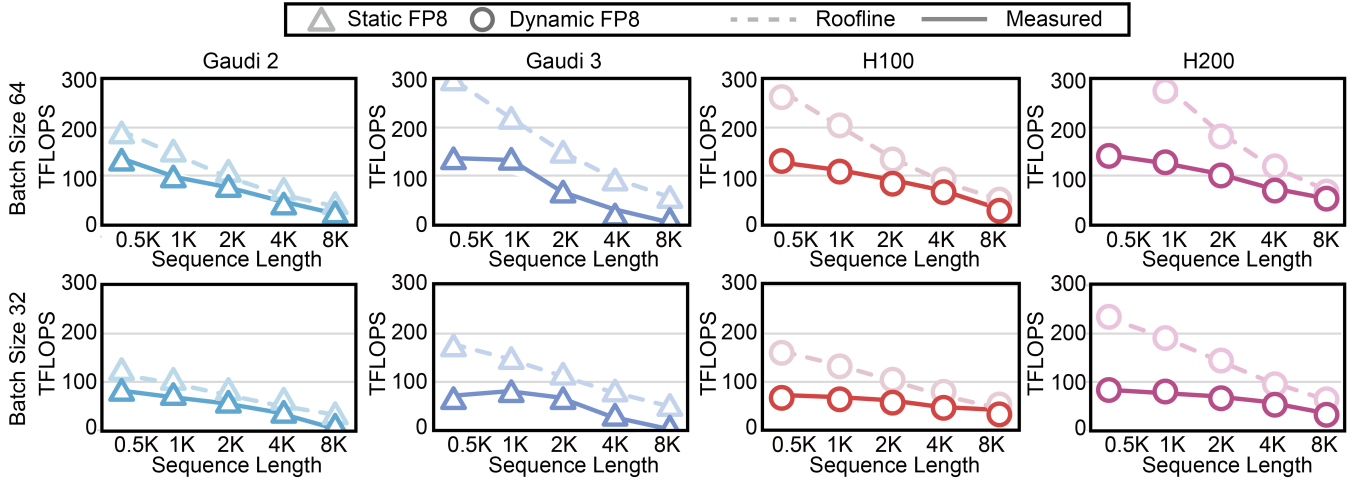


Fig. 6. Comparison between measured and roofline throughputs obtained from hardware specifications across varying sequence lengths and batch sizes for the Llama v3.1 8B Instruct model. The dashed lines indicate the roofline estimates, whereas the solid lines represent the measured TFLOPS with FP8 quantization.

### B. Decode Phase

The decoding phase has become the primary bottleneck in end-to-end inference for autoregressive LLMs. As recent “reasoning” models [8] often generate hundreds or even thousands of tokens to produce high-quality responses, the duration of the decode phase increasingly dominates total inference time. Optimizing decoding is therefore essential to reduce latency and improve overall throughput.

Figure 5 presents a comparison of decode throughput across four accelerators. BF16 and static FP8 scaling are used on HPUs, whereas BF16 and dynamic FP8 scaling are compared for GPUs. While software optimization differences exist across devices, our comparison focuses on the best-performing configurations for each, specifically those showing higher TFLOPS than their respective BF16 baselines. A key observation is that the Gaudi 2 achieves comparable or even higher throughput in FP8 than the BF16 throughput of the other devices, all of which have higher hardware specifications. This result underscores the effectiveness of adopting low-precision FP8 for memory-bound workloads, often yielding greater efficiency than relying solely on newer or higher-performance hardware.

However, the performance gains depend heavily on the underlying hardware architecture. For example, Gaudi 2 shows a substantial FP8 improvement of over 65%, while NVIDIA GPUs yield more modest gains of under 25%. The Gaudi 3 also exhibits unstable FP8 throughput, performing well on short sequences but degrading sharply on longer ones. These results suggest that fully leveraging FP8 requires co-design between hardware and software.

As shown in Figure 6, the discrepancy becomes more evident when comparing theoretical roofline performance with actual throughput. On the Gaudi 2, the measured throughput closely aligns with the theoretical roofline, whereas other accelerators exhibit noticeable gaps. In practice, lower-end devices can match or even exceed the performance of higher-end counterparts using FP8, offering a significant TCO advantage.

## VI. INSIGHTS INTO HARDWARE DESIGN

### A. LLM Decoding and Thin GEMM Throughput

The dominant workload during LLM decoding is the thin GEMM, making thin GEMM throughput the dominant influence on overall inference latency. As shown in Equation 8, the decoding stage at short sequence lengths ( $s < h$ ) is dominated by linear operations, while longer sequences are increasingly dominated by attention. Although LLM sizes continue to scale, their hidden dimensions grow at a much slower rate. For example, Llama v3.1 8B has a hidden size of 4096, whereas Llama v3.3 70B increases it only to 8192. Tensor parallelism (TP), which is commonly employed to reduce latency and memory overhead, further partitions model weight matrices into smaller submatrices. The growing adoption of fine-grained Mixture-of-Experts (MoE) models [17, 49] also contributes to this trend, as MoE models consist of a large number of experts with relatively small hidden dimension sizes.

Table III presents GEMM TFLOPS in a setting where the dimension of the matrix  $M$  is significantly smaller than  $K$  and  $N$ . This setup is similar to the thin GEMM condition faced during decoding with a batch size of  $M$ . Row-wise scaling is used for the FP8 GEMMs. Quantization is excluded from the measurement. Both input matrices are in FP8 while the output matrix is in BF16.

Throughput scales linearly with  $M$  on all devices, but Gaudi HPUs tend to achieve higher throughput than NVIDIA GPUs for both BF16 and especially FP8. Compared to their performance on large GEMMs, NVIDIA GPUs show notably lower throughput than their specifications under these thin GEMM conditions. FP8 and BF16 throughputs for the NVIDIA GPUs are nearly identical, failing to reflect the expected performance gains from lower precision. In contrast, Gaudi HPUs exhibit an FP8 throughput approximately double that of BF16, aligning well with expectations.

Figure 7 presents the MFU of thin GEMM operations, computed using the method described above. While the Gaudi 3



TABLE III  
THIN GEMM THROUGHPUTS (IN TFLOPS) OF THE GAUDI 2, GAUDI 3, H100, AND H200

GEMM TFLOPS	K, N	2048				4096			
Shape: (M,K,N)	M	8	16	32	64	8	16	32	64
Gaudi 2	BF16	13.1	25.8	50.4	110.5	18.8	37.3	73.9	145.0
	FP8	24.6	47.7	88.8	162.2	35.7	67.8	131.4	252.5
Gaudi 3	BF16	16.7	34.6	45.3	130.9	26.9	53.6	106.0	203.0
	FP8	24.6	47.4	66.9	157.1	49.9	99.1	193.5	370.9
H100	BF16	5.3	10.7	19.9	41.2	14.7	28.5	68.3	133.2
	FP8	5.3	10.4	21.0	41.9	15.5	31.0	63.8	120.5
H200	BF16	6.2	12.1	24.2	48.0	17.8	34.4	67.9	158.2
	FP8	6.7	13.4	26.5	53.3	18.3	36.7	72.7	151.3

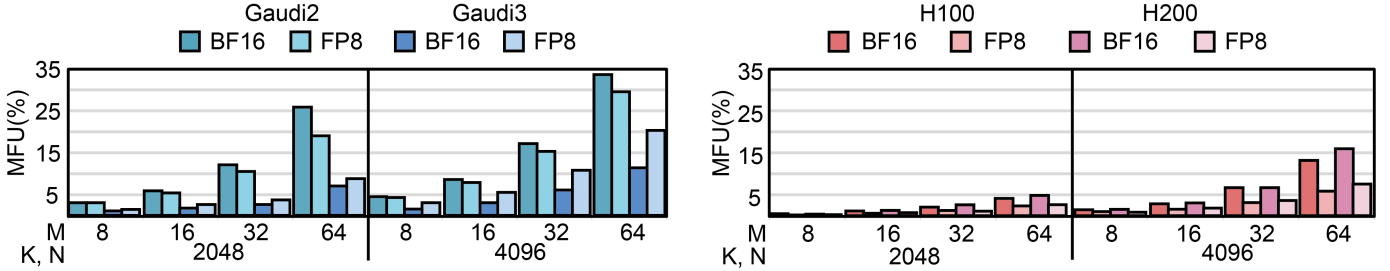


Fig. 7. Thin GEMM MFU comparison for both BF16 and FP8. The Gaudi HPUs maintain a similar MFU for BF16 and FP8 of similar shapes, while there is a noticeable drop for the NVIDIA GPUs. The MFU differences at the same shapes are enough to provide superior TFLOPS for the Gaudi HPUs over the NVIDIA GPUs as shown in Table III.

exhibits some fluctuation, the overall MFU of Gaudi HPUs consistently exceeds that of NVIDIA GPUs. Especially in the case of the Gaudi 2, despite its having a lower peak TFLOPS and memory bandwidth than both the H100 and the H200, it has a higher absolute throughput for most of the matrix shapes in Table III. This indicates that HPUs achieve more effective performance in thin GEMM workloads primarily due to their higher MFU, which enables more efficient utilization of compute units for memory-bound computations. An interesting observation is that the Gaudi 3 has a lower MFU than the Gaudi 2, with the Gaudi 3 sometimes even having a lower absolute throughput as well.

#### B. MME Differences Between GPUs and HPUs

Although FP8 offers up to double the throughput of BF16 or FP16, suboptimal input/output pipelining or memory access patterns can severely bottleneck overall throughput, even if the compute units are capable of fast execution. Unlike large matrix-matrix multiplications, thin GEMMs fail to fully utilize computing units. Moreover, the inefficiency that derives from hardware utilization increases as low data precision is adopted. Therefore, to operate datacenters efficiently, it is crucial to understand how specific accelerators perform in scenarios involving thin GEMM and low-precision computations.

The differences in FP8 thin GEMM performance are likely attributed to the architectural differences of the accelerators. Figure 8 depicts the differences between the MME architectures of Gaudi HPUs and those of other commercial hardware solutions. In architectures that rely on several small units, each

unit consumes input data in every cycle, incurring significant overhead in unit-to-unit data movement. In contrast, one large MME consumes a much smaller amount of input data per cycle and requires less expensive ALU-to-ALU communication within a whole MME. As a result, Gaudi HPUs require fewer input elements per cycle to fully utilize compute resources, thereby reducing first-level memory bandwidth requirements and improving efficiency [48, 50].

Furthermore, Figure 9 illustrates the reconfigurable MME sizes of Gaudi HPUs. Gaudi HPUs leverage a graph compiler to dynamically reconfigure the MME size based on the target GEMM dimensions, optimizing resource utilization [47]. While the Gaudi HPU architecture contains MMEs with size  $256 \times 256$ , they can be folded and integrated in different sizes with a minimum width of 128. This flexibility allows the hardware to adapt to a wide range of GEMM dimensions in practice, offering substantial potential for improving LLM inference efficiency.

#### C. Exponential Function Optimization

While the Gaudi 2 & 3 outperform the H100 and H200 in the LLM decode phase for short sequence lengths of below 512, their throughput gains diminish at longer sequence lengths. We find that this decline is primarily due to the absence of dedicated special function units (SFUs, also referred to as multi-function units, or MUFUs) in Gaudi HPUs to accelerate exponential calculations in the softmax.

Although GEMM operations that leverage tensor cores dominate LLM workloads, specialized functions such as soft-

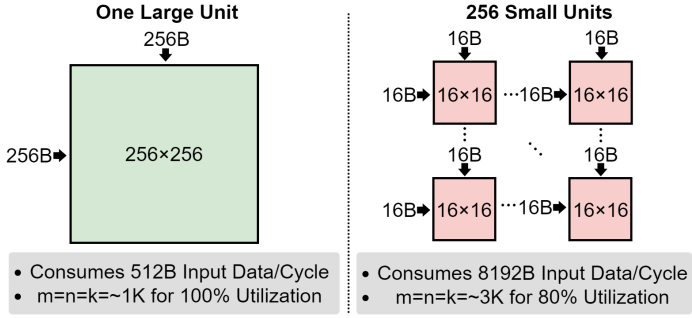


Fig. 8. Gaudi HPUs employ a few large systolic array units in the MMEs, unlike NVIDIA GPUs, which employ many small units across streaming multiprocessors.

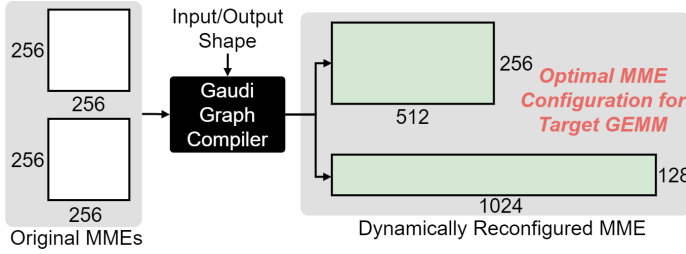


Fig. 9. Dynamically reconfigurable MME architecture on Gaudi HPUs for target GEMM size optimization. The minimum size of the reconfigured MME unit is 128 elements for both BF16 and FP8.

max and SiLU are also necessary. During LLM inference, SFUs perform the exponential computations in these functions efficiently. For decoding workloads, the ratio of exponential computations relative to GEMM computations increases in proportion to the sequence length. As a result, the softmax operation becomes a bottleneck for decoding at longer sequence lengths. GPUs equipped with SFUs can process exponential functions on SFUs while simultaneously executing GEMMs on tensor cores to pipeline the workload.

In contrast, both the Gaudi 2 & 3 have a disadvantage in that they lack SFUs and must handle exponential computations via their TPC cores. They also have a lower ratio of vector core compute relative to matrix computation compared to the H200. Peak TPC core BF16 throughput is 11 TFLOPS for the Gaudi 2 and 28.7 TFLOPS for the Gaudi 3, whereas the H200 has 133.8 TFLOPS BF16 CUDA core throughput and includes separate SFU cores. Because of this, the softmax becomes a greater bottleneck for the Gaudi during decoding. This implies that despite the notable efficiency of thin GEMMs in Gaudi HPUs, exponential function calculations bottleneck HPU decoding throughput for long sequences, as the softmax computation scales  $O(BS)$  for batch size  $B$  and sequence length  $S$  during decoding.

Gaudi HPUs also incorporate an embedded look-up table (LUT), which could store precomputed special function values via piecewise linear approximation. If the LUT offers sufficiently low access latency and can hold a large enough range of values, it may be a valid substitute for SFUs. However, Gaudi

HPUs currently lack software support for easily programming the LUTs. Although it has potential in improving performance with long sequences, the limited software stack constrains its practical effectiveness.

#### D. Power Capping

Our experiments in Section V showed that although the Gaudi 2 could often outperform the H100 and H200 on memory-bound thin GEMMs, the Gaudi 3 sometimes even fell behind the Gaudi 2. An investigation into the root cause found that the Gaudi 3 had low throughput because of power throttling within the chip to adhere to the TDP constraints. On closer inspection, we discovered that the Gaudi 3 reached its TDP of 900W even for thin GEMMs. The reason that it had a lower prefill throughput than the H200, despite having a higher peak TFLOPS, was also because power throttling reduced the achieved GEMM throughput of the Gaudi 3.

Although setting the power cap too low as in the case of the Gaudi 3 can cause problems due to having too little power available, prior work [51] has found that power capping at appropriate levels can improve hardware reliability and mean time between failures. Power capping can also reduce infrastructure costs by allowing more servers to be placed in a single datacenter rack. Therefore, power capping is a viable strategy if the throughput decrease is less than the TCO gain.

TABLE IV  
DECODE TFLOPS WITH AND WITHOUT A 400W CAP ON THE H200

Length	Llama v3.1 8B (BS=64)			Llama v3.3 70B (BS=4)		
	W/O	W/	Difference	W/O	W/	Difference
512	141	132	7%	23	19	19%
1024	126	111	11%	23	19	17%
2048	105	86	18%	24	19	21%
4096	76	64	15%	21	19	9 %
8192	56	40	28%	23	18	21%

Table IV compares the decode throughput of the H200 across varying sequence lengths under its default 700W TDP and when applying a power cap of 400W for Llama 8B and 70B models with batch sizes of 64 and 4, respectively. Although previous works such as SplitWise [15] found that power capping did not slow decoding at 400W, we find that the same power cap causes noticeable throughput degradation, possibly because framework updates have made LLM decoding more efficient.

A limitation of currently available power capping solutions is that they operate on a single card and cannot share their cap. However, considering that the primary purpose of power capping is to limit the peak power consumption of the rack, it would be beneficial to be able to pool the cap across many devices. However, this functionality is only available in Grace superchips with automatic power steering capabilities.

## VII. THROUGHPUT SHIFTS THE TCO BALANCE

### A. Hardware Characteristics Related to Data Precision

We now summarize how hardware support for low-precision computation influences the cost-efficiency of LLM inference, as captured by our TCO model. In the decoding phase of LLM inference, which often dominates total latency, Gaudi 2 achieves nearly 50% higher throughput using FP8 quantization than BF16, while the H100 and H200 show little to no improvement. This results in an upward shift along the y-axis in the TCO table shown in Figure 2, moving the evaluation point into the green region, which indicates the improved cost efficiency of the Gaudi 2. Conversely, in long-sequence scenarios, the Gaudi 2 & 3 suffer from softmax bottlenecks due to the absence of a dedicated SFU or alternative workaround, reducing  $R_{Th}$  and shifting the evaluation point downward into the red region, where choosing H100 and H200 becomes more cost-effective solution.

### B. Workload Characteristics

In practical deployment, inference services must satisfy diverse service-level objectives (SLOs) depending on the application. For example, latency-sensitive workloads such as real-time voice dialogue systems require near-instantaneous responses, making low-latency SLOs essential. In contrast, creative generation tasks such as image or slide synthesis can tolerate longer delays in exchange for higher output quality. These differences in performance requirements directly affect achievable throughput, thus resulting in different vertical positions on the TCO table.

To support such a variety of workloads, datacenters are required to deploy inference systems that can efficiently serve both lightweight and large-scale models. SLO-aware inference system optimization frameworks, such as [52, 53], dynamically adjust resource allocation and engine parameters to handle multi-SLO environments. As a result, even for the same hardware configuration, the evaluation point on the TCO table may shift depending on the workload.

In this context, hardware selection is guided not by a single evaluation point, but by the overall distribution of expected workloads. Since each application maps to a unique point on the TCO surface, robust deployment decisions require analyzing these points collectively. The optimal hardware is the one that maintains strong cost-efficiency across the majority of operating scenarios, rather than excelling in only a narrow performance region.

## VIII. LIMITATIONS

In this study, we present a scalable framework for comparing AI accelerator options in terms of datacenter TCO. However, our study has several limitations.

First, we did not discuss KV cache quantization [54, 55], as this is a memory-saving technique, distinct from GEMM computation. While KV cache quantization can improve decode throughput by reducing the memory read from DRAM, the GEMM computations within the attention operation are

conducted in BF16 to preserve accuracy, even in models such as DeepSeek-V3 [17] where linear layers use FP8 quantization.

Second, we concentrate on evaluating performance on a single device without factoring in the communication costs between devices or nodes. This simplifies the analysis because disaggregated inference allows devices to focus on a single workload. However, it limits our analysis of tensor parallelism, which is dependent on low-latency communications. For example, tensor parallelism can be made more efficient by asynchronously overlapping the GEMM computations with the buffer communications [56], but asynchronous tensor parallelism is unavailable for the Gaudi as of the time of writing.

Third, our analysis focuses on Llama-based dense models [57]. As such, the results may not directly generalize to other workloads, particularly those involving MoE inference. We intentionally simplify our analysis to focus on a single device with a uniform workload, even though workload imbalances at both the node and device levels are a critical issue in MoE inference [58], which requires sophisticated load balancing for the experts. However, analyzing complex workloads requires breaking them down into their components, which our work has attempted to do. Moreover, as efficient MoE inference requires disaggregation [17], our analysis of the component workloads serves as a starting point for further investigation into more sophisticated deployments. Also, note that MoE inference reduces the average batch size of each expert by the ratio of active experts to the total number of experts, heightening the importance of thin GEMM analysis.

## IX. CONCLUSION

The incredible progress in LLM capabilities seen over the last few years has ushered in an unprecedented buildup of datacenter capacity as corporations and nation states spend hundreds of billions of dollars to hasten the adoption of AI. In this study, we present a scalable framework for comparing AI accelerator options in terms of datacenter TCO. Using our model, we examine two key factors that influence throughput and are directly connected to the TCO: hardware characteristics related to numerical precision and workload-specific behavior in LLM inference. We evaluate four AI accelerators: the Intel Gaudi 2 & 3 and the NVIDIA H100 & H200, and analyze their behavior under FP8 quantization.

Recent AI accelerators primarily focus on maximizing raw computational performance, typically measured in peak TFLOPS. However, our study highlights that such a singular emphasis may result in inefficient AI datacenter management. From the perspective of CSPs who deploy LLM services, throughput measurements on their target workloads, as well as considerations such as power efficiency, are also critical. We highlight the key role of thin GEMMs and FP8 quantization in LLM decoding, a highly important aspect of optimizing AI datacenter TCO. We hope that the insights provided in this work will inform practical deployment decisions and guide future accelerator design efforts toward more efficient and workload-aware LLM inference at scale.

# REFERENCES

- [1] OpenAI. Announcing the stargate project, 2025. URL <https://openai.com/index/announcing-the-stargate-project>.
- [2] OpenAI. Stargate advances with 4.5 gw partnership with oracle, 2025. URL <https://openai.com/index/stargate-advances-with-partnership-with-oracle>.
- [3] Meta. The largest meta data center yet brings big impact to louisiana, 2024. URL <https://datacenters.atmeta.com/richland-parish-data-center>.
- [4] U.S. Department of Energy Office of Nuclear Energy. How much power does a nuclear reactor produce?, 2021. URL <https://www.energy.gov/ne/articles/infographic-how-much-power-does-nuclear-reactor-produce>.
- [5] City of New York Mayor’s Office of Climate & Environmental Justice. Building a clean, resilient, and affordable energy system., 2025. URL <https://climate.cityofnewyork.us/subtopics/systems>.
- [6] OpenAI. Introducing openai o1, 2024. URL <https://openai.com/o1>.
- [7] Anthropic. Claude 3.7 sonnet, 2025. URL <https://www.anthropic.com/news/claude-3-7-sonnet>.
- [8] DeepSeek-AI. Deepseek-r1: Incentivizing reasoning capability in llms via reinforcement learning, 2025. URL <https://arxiv.org/abs/2501.12948>.
- [9] An Yang, Anfeng Li, Baosong Yang, Beichen Zhang, Binyuan Hui, Bo Zheng, Bowen Yu, Chang Gao, Chengen Huang, Chenxu Lv, Chujie Zheng, Dayiheng Liu, Fan Zhou, Fei Huang, Feng Hu, Hao Ge, Haoran Wei, Huan Lin, Jialong Tang, Jian Yang, Jianhong Tu, Jianwei Zhang, Jianxin Yang, Jiayi Yang, Jing Zhou, Jingren Zhou, Junyang Lin, Kai Dang, Keqin Bao, Kexin Yang, Le Yu, Lianghao Deng, Mei Li, Mingfeng Xue, Mingze Li, Pei Zhang, Peng Wang, Qin Zhu, Rui Men, Ruize Gao, Shixuan Liu, Shuang Luo, Tianhao Li, Tianyi Tang, Wenbiao Yin, Xingzhang Ren, Xinyu Wang, Xinyu Zhang, Xuancheng Ren, Yang Fan, Yang Su, Yichang Zhang, Yinger Zhang, Yu Wan, Yuqiong Liu, Zekun Wang, Zeyu Cui, Zhenru Zhang, Zhipeng Zhou, and Zihan Qiu. Qwen3 technical report, 2025. URL <https://arxiv.org/abs/2505.09388>.
- [10] Paulius Micikevicius, Dusan Stosic, Neil Burgess, Marius Cornea, Pradeep Dubey, Richard Grisenthwaite, Sangwon Ha, Alexander Heinecke, Patrick Judd, John Kamalu, Naveen Mellempudi, Stuart Oberman, Mohammad Shoeybi, Michael Siu, and Hao Wu. Fp8 formats for deep learning, 2022. URL <https://arxiv.org/abs/2209.05433>.
- [11] Joonhyung Lee, Shmulik Markovich-Golan, Daniel Ohayon, Yair Hanani, Gunho Park, Byeongwook Kim, Asaf Karnieli, Uri Livne, Haihao Shen, Tai Huang, Se Jung Kwon, and Dongsoo Lee. Faster inference of llms using fp8 on the intel gaudi, 2025. URL <https://arxiv.org/abs/2503.09975>.
- [12] Yujun Lin, Haotian Tang, Shang Yang, Zhekai Zhang, Guangxuan Xiao, Chuang Gan, and Song Han. Qserve: W4a8kv4 quantization and system co-design for efficient llm serving. *arXiv preprint arXiv:2405.04532*, 2024.
- [13] Saleh Ashkboos, Amirkeivan Mohtashami, Maximilian L. Croci, Bo Li, Pashmina Cameron, Martin Jaggi, Dan Alistarh, Torsten Hoeffler, and James Hensman. Quarot: Outlier-free 4-bit inference in rotated LLMs. In *The Thirty-eighth Annual Conference on Neural Information Processing Systems*, 2024. URL <https://openreview.net/forum?id=dfqsW38v1X>.
- [14] Guangxuan Xiao, Ji Lin, Mickael Seznec, Hao Wu, Julien Demouth, and Song Han. SmoothQuant: Accurate and efficient post-training quantization for large language models. In Andreas Krause, Emma Brunskill, Kyunghyun Cho, Barbara Engelhardt, Sivan Sabato, and Jonathan Scarlett, editors, *Proceedings of the 40th International Conference on Machine Learning*, volume 202 of *Proceedings of Machine Learning Research*, pages 38087–38099. PMLR, 23–29 Jul 2023. URL <https://proceedings.mlr.press/v202/xiao23c.html>.
- [15] Pratyush Patel, Esha Choukse, Chaojie Zhang, Aashaka Shah, Inigo Goiri, Saeed Maleki, and Ricardo Bianchini. Splitwise: Efficient generative llm inference using phase splitting. In *2024 ACM/IEEE 51st Annual International Symposium on Computer Architecture (ISCA)*, pages 118–132, 2024. doi: 10.1109/ISCA59077.2024.00019.
- [16] Tyler Griggs, Xiaoxuan Liu, Jiaxiang Yu, Doyoung Kim, Wei-Lin Chiang, Alvin Cheung, and Ion Stoica. Mélange: Cost efficient large language model serving by exploiting gpu heterogeneity, 2024. URL <https://arxiv.org/abs/2404.14527>.
- [17] DeepSeek-AI. Deepseek-v3 technical report, 2024. URL <https://arxiv.org/abs/2412.19437>.
- [18] Neil Burgess, Jelena Milanovic, Nigel Stephens, Konstantinos Monachopoulos, and David Mansell. Bfloat16 processing for neural networks. In *2019 IEEE 26th Symposium on Computer Arithmetic (ARITH)*, pages 88–91, 2019. doi: 10.1109/ARITH.2019.00022.
- [19] Aakanksha Chowdhery, Sharan Narang, Jacob Devlin, Maarten Bosma, Gaurav Mishra, Adam Roberts, Paul Barham, Hyung Won Chung, Charles Sutton, Sebastian Gehrmann, Parker Schuh, Kensen Shi, Sashank Tsvyashchenko, Joshua Maynez, Abhishek Rao, Parker Barnes, Yi Tay, Noam Shazeer, Vinodkumar Prabhakaran, Emily Reif, Nan Du, Ben Hutchinson, Reiner Pope, James Bradbury, Jacob Austin, Michael Isard, Guy Gur-Ari, Pengcheng Yin, Toju Duke, Anselm Levskaya, Sanjay Ghemawat, Sunipa Dev, Henryk Michalewski, Xavier Garcia, Vedant Misra, Kevin Robinson, Liam Fedus, Denny Zhou, Daphne Ippolito, David Luan, Hyeontaek Lim, Barret Zoph, Alexander Spiridonov, Ryan Sepassi, David Dohan, Shivani Agrawal, Mark Omernick, Andrew M. Dai, Thanumalayan Sankaranarayanan Pillai, Marie Pellat, Aitor Lewkowycz, Erica Moreira, Rewon Child, Oleksandr Polozov, Katherine Lee, Zongwei Zhou, Xuezhi Wang, Brennan Saeta, Mark Diaz, Orhan Firat, Michele Catasta, Jason Wei, Kathy Meier-Hellstern, Dou-

- glas Eck, Jeff Dean, Slav Petrov, and Noah Fiedel. Palm: scaling language modeling with pathways. *J. Mach. Learn. Res.*, 24(1), January 2023. ISSN 1532-4435.
- [20] Deepak Narayanan, Mohammad Shoeybi, Jared Casper, Patrick LeGresley, Mostofa Patwary, Vijay Korthikanti, Dmitri Vainbrand, Prethvi Kashinkunti, Julie Bernauer, Bryan Catanzaro, Amar Phanishayee, and Matei Zaharia. Efficient large-scale language model training on gpu clusters using megatron-lm. In *Proceedings of the International Conference for High Performance Computing, Networking, Storage and Analysis*, SC '21, New York, NY, USA, 2021. Association for Computing Machinery. ISBN 9781450384421. doi: 10.1145/3458817.3476209. URL <https://doi.org/10.1145/3458817.3476209>.
- [21] Norman P. Jouppi, Cliff Young, Nishant Patil, David Patterson, Gaurav Agrawal, Raminder Bajwa, Sarah Bates, Suresh Bhatia, Nan Boden, Al Borchers, Rick Boyle, Pierre-luc Cantin, Clifford Chao, Chris Clark, Jeremy Coriell, Mike Daley, Matt Dau, Jeffrey Dean, Ben Gelb, Tara Vazir Ghaemmaghami, Rajendra Gotipati, William Gulland, Robert Hagmann, C. Richard Ho, Doug Hogberg, John Hu, Robert Hundt, Dan Hurt, Julian Ibarz, Aaron Jaffey, Alek Jaworski, Alexander Kaplan, Harshit Khaitan, Daniel Killebrew, Andy Koch, Naveen Kumar, Steve Lacy, James Laudon, James Law, Diemthu Le, Chris Leary, Zhuyuan Liu, Kyle Lucke, Alan Lundin, Gordon MacKean, Adriana Maggiore, Maire Mahony, Kieran Miller, Rahul Nagarajan, Ravi Narayanaswami, Ray Ni, Kathy Nix, Thomas Norrie, Mark Omernick, Narayana Penukonda, Andy Phelps, Jonathan Ross, Matt Ross, Amir Salek, Emad Samadiani, Chris Severn, Gregory Sizikov, Matthew Snelham, Jed Souter, Dan Steinberg, Andy Swing, Mercedes Tan, Gregory Thorson, Bo Tian, Horia Toma, Erick Tuttle, Vijay Vasudevan, Richard Walter, Walter Wang, Eric Wilcox, and Doe Hyun Yoon. In-datacenter performance analysis of a tensor processing unit. *SIGARCH Comput. Archit. News*, 45(2):1–12, June 2017. ISSN 0163-5964. doi: 10.1145/3140659.3080246. URL <https://doi.org/10.1145/3140659.3080246>.
- [22] Yan Cui, Charles Ingalz, Tianyi Gao, and Ali Heydari. Total cost of ownership model for data center technology evaluation. In *2017 16th IEEE Intersociety Conference on Thermal and Thermomechanical Phenomena in Electronic Systems (ITherm)*, pages 936–942, 2017. doi: 10.1109/ITHERM.2017.7992587.
- [23] NVIDIA. Nvidia tesla v100 gpu architecture v1.1, 2017. URL <https://images.nvidia.com/content/volta-architecture/pdf/volta-architecture-whitepaper.pdf>. Accessed: 2025-08-014.
- [24] NVIDIA. Nvidia a100 tensor core gpu architecture v1.0, 2020. URL <https://images.nvidia.com/aem-dam/en-zz/Solutions/data-center/nvidia-ampere-architecture-whitepaper.pdf>. Accessed: 2025-07-24.
- [25] NVIDIA. Nvidia h100 tensor core gpu architecture v1.04, 2022. URL <https://resources.nvidia.com/en-us-hopper-architecture/nvidia-h100-tensor-c>. Accessed: 2025-07-24.
- [26] NVIDIA. Nvidia h200 tensor core gpu, 2023. URL <https://resources.nvidia.com/en-us-data-center-overview-mc/en-us-data-center-overview/hpc-datasheet-sc23-h200>. Accessed: 2025-07-24.
- [27] NVIDIA. Nvidia blackwell architecture technical brief v2.0, 2025. URL <https://resources.nvidia.com/en-us-blackwell-architecture>. Accessed: 2025-07-24.
- [28] Open Compute Project. Ocp microscaling formats (mx) specification v1, 2023. URL <https://www.opencompute.org/documents/ocp-microscaling-formats-mx-v1-0-spec-final-pdf>.
- [29] Haihao Shen, Naveen Mellempudi, Xin He, Qun Gao, Chang Wang, and Mengni Wang. Efficient post-training quantization with fp8 formats. In P. Gibbons, G. Pekhimenko, and C. De Sa, editors, *Proceedings of Machine Learning and Systems*, volume 6, pages 483–498, 2024.
- [30] Badreddine Noune, Philip Jones, Daniel Justus, Dominic Masters, and Carlo Luschi. 8-bit numerical formats for deep neural networks, 2022. URL <https://arxiv.org/abs/2206.02915>.
- [31] Haozheng Fan, Hao Zhou, Guangtai Huang, Parameswaran Raman, Xinwei Fu, Gaurav Gupta, Dhananjay Ram, Yida Wang, and Jun Huan. HLAT: High-quality Large Language Model Pre-trained on AWS Trainium. In *2024 IEEE International Conference on Big Data (BigData)*, pages 2100–2109, Los Alamitos, CA, USA, December 2024. IEEE Computer Society. doi: 10.1109/BigData62323.2024.10825098. URL <https://doi.ieeecomputersociety.org/10.1109/BigData62323.2024.10825098>.
- [32] El-Mehdi El Arar, Devan Sohler, Pablo de Oliveira Castro, and Eric Petit. Stochastic rounding variance and probabilistic bounds: A new approach. *SIAM Journal on Scientific Computing*, 45(5):C255–C275, 2023. doi: 10.1137/22M1510819. URL <https://doi.org/10.1137/22M1510819>.
- [33] Elias Frantar and Dan Alistarh. Sparsegpt: massive language models can be accurately pruned in one-shot. In *Proceedings of the 40th International Conference on Machine Learning, ICML'23*. JMLR.org, 2023.
- [34] Mingjie Sun, Zhuang Liu, Anna Bair, and J Zico Kolter. A simple and effective pruning approach for large language models. In *The Twelfth International Conference on Learning Representations*, 2024. URL <https://openreview.net/forum?id=PxoFut3dWW>.
- [35] Jianlin Su, Murtadha Ahmed, Yu Lu, Shengfeng Pan, Wen Bo, and Yunfeng Liu. Roformer: Enhanced transformer with rotary position embedding. *Neurocomput.*, 568(C), February 2024. ISSN 0925-2312. doi: 10.1016/j.neucom.2023.127063. URL <https://doi.org/10.1016/j.neucom.2023.127063>.
- [36] Haonan Wang, Qian Liu, Chao Du, Tongyao Zhu, Cunxiao Du, Kenji Kawaguchi, and Tianyu Pang. When precision meets position: BFloat16 breaks down roPE in



- long-context training. *Transactions on Machine Learning Research*, 2025. ISSN 2835-8856. URL <https://openreview.net/forum?id=gwXfZ3xkUq>.
- [37] Yilong Zhao, Chien-Yu Lin, Kan Zhu, Zihao Ye, Lequn Chen, Size Zheng, Luis Ceze, Arvind Krishnamurthy, Tianqi Chen, and Baris Kasikci. Atom: Low-bit quantization for efficient and accurate llm serving. *Proceedings of Machine Learning and Systems*, 6:196–209, 2024.
  - [38] Mingjie Sun, Xinlei Chen, J. Zico Kolter, and Zhuang Liu. Massive activations in large language models. *arXiv preprint arXiv:2402.17762*, 2024.
  - [39] Zechun Liu, Changsheng Zhao, Igor Fedorov, Bilge Soran, Dhruv Choudhary, Raghuraman Krishnamoorthi, Vikas Chandra, Yuandong Tian, and Tijmen Blankevoort. Spinqant–llm quantization with learned rotations. *arXiv preprint arXiv:2405.16406*, 2024.
  - [40] Yinmin Zhong, Shengyu Liu, Junda Chen, Jianbo Hu, Yibo Zhu, Xuanzhe Liu, Xin Jin, and Hao Zhang. Dist-serve: Disaggregating prefill and decoding for goodput-optimized large language model serving. In *OSDI*, pages 193–210, 2024. URL <https://www.usenix.org/conference/osdi24/presentation/zhong-yinmin>.
  - [41] Woosuk Kwon, Zhuohan Li, Siyuan Zhuang, Ying Sheng, Lianmin Zheng, Cody Hao Yu, Joseph E. Gonzalez, Hao Zhang, and Ion Stoica. Efficient memory management for large language model serving with pagedattention. In *Proceedings of the ACM SIGOPS 29th Symposium on Operating Systems Principles*, 2023.
  - [42] NVIDIA. Tensorrt-llm, 2023. URL <https://github.com/NVIDIA/TensorRT-LLM>.
  - [43] Joshua Ainslie, James Lee-Thorp, Michiel de Jong, Yury Zemlyanskiy, Federico Lebron, and Sumit Shinghani. GQA: Training generalized multi-query transformer models from multi-head checkpoints. In *The 2023 Conference on Empirical Methods in Natural Language Processing*, 2023. URL <https://openreview.net/forum?id=hmOwOZWzYE>.
  - [44] DeepSeek-AI, Aixin Liu, Bei Feng, Bin Wang, Bingxuan Wang, Bo Liu, Chenggang Zhao, Chengqi Deng, Chong Ruan, Damai Dai, Daya Guo, Dejian Yang, Deli Chen, Dongjie Ji, Erhang Li, Fangyun Lin, Fuli Luo, Guangbo Hao, Guanting Chen, Guowei Li, H. Zhang, Hanwei Xu, Hao Yang, Haowei Zhang, Honghui Ding, Huajian Xin, Huazuo Gao, Hui Li, Hui Qu, J. L. Cai, Jian Liang, Jianzhong Guo, Jiaqi Ni, Jiashi Li, Jin Chen, Jingyang Yuan, Junjie Qiu, Junxiao Song, Kai Dong, Kaige Gao, Kang Guan, Lean Wang, Lecong Zhang, Lei Xu, Leyi Xia, Liang Zhao, Liyue Zhang, Meng Li, Miao-jun Wang, Mingchuan Zhang, Minghua Zhang, Minghui Tang, Mingming Li, Ning Tian, Panpan Huang, Peiyi Wang, Peng Zhang, Qihao Zhu, Qinyu Chen, Qiushi Du, R. J. Chen, R. L. Jin, Ruiqi Ge, Ruizhe Pan, Runxin Xu, Ruyi Chen, S. S. Li, Shanghao Lu, Shangyan Zhou, Shanhuang Chen, Shaoqing Wu, Shengfeng Ye, Shirong Ma, Shiyu Wang, Shuang Zhou, Shuiping Yu, Shunfeng Zhou, Size Zheng, T. Wang, Tian Pei, Tian Yuan, Tianyu Sun, W. L. Xiao, Wangding Zeng, Wei An, Wen Liu, Wenfeng Liang, Wenjun Gao, Wentao Zhang, X. Q. Li, Xiangyue Jin, Xianzu Wang, Xiao Bi, Xiaodong Liu, Xiaohan Wang, Xiaojin Shen, Xiaokang Chen, Xiaosha Chen, Xiaotao Nie, Xiaowen Sun, Xiaoxiang Wang, Xin Liu, Xin Xie, Xingkai Yu, Xinnan Song, Xinyi Zhou, Xinyu Yang, Xuan Lu, Xuecheng Su, Y. Wu, Y. K. Li, Y. X. Wei, Y. X. Zhu, Yanhong Xu, Yanping Huang, Yao Li, Yao Zhao, Yaofeng Sun, Yaohui Li, Yaohui Wang, Yi Zheng, Yichao Zhang, Yiliang Xiong, Yilong Zhao, Ying He, Ying Tang, Yishi Piao, Yixin Dong, Yixuan Tan, Yiyuan Liu, Yongji Wang, Yongqiang Guo, Yuchen Zhu, Yuduan Wang, Yuheng Zou, Yukun Zha, Yunxian Ma, Yuting Yan, Yuxiang You, Yuxuan Liu, Z. Z. Ren, Zehui Ren, Zhangli Sha, Zhe Fu, Zhen Huang, Zhen Zhang, Zhenda Xie, Zhewen Hao, Zhihong Shao, Zhiyuan Wen, Zhipeng Xu, Zhongyu Zhang, Zhuoshu Li, Zihan Wang, Zihui Gu, Zilin Li, and Ziwei Xie. Deepseek-v2: A strong, economical, and efficient mixture-of-experts language model, 2024. URL <https://arxiv.org/abs/2405.04434>.
  - [45] Jason Ansel, Edward Yang, Horace He, Natalia Gimelshein, Animesh Jain, Michael Voznesensky, Bin Bao, Peter Bell, David Berard, Evgeni Burovski, Geeta Chauhan, Anjali Chourdia, Will Constable, Alban Desmaison, Zachary DeVito, Elias Ellison, Will Feng, Jiong Gong, Michael Gschwind, Brian Hirsh, Sherlock Huang, Kshiteej Kalambarkar, Laurent Kirsch, Michael Lazos, Mario Lezcano, Yanbo Liang, Jason Liang, Yinghai Lu, C. K. Luk, Bert Maher, Yunjie Pan, Christian Puhresch, Matthias Reso, Mark Saroufim, Marcos Yukio Siraichi, Helen Suk, Shunting Zhang, Michael Suo, Phil Tillet, Xu Zhao, Eikan Wang, Keren Zhou, Richard Zou, Xiaodong Wang, Ajit Mathews, William Wen, Gregory Chanan, Peng Wu, and Soumith Chintala. Pytorch 2: Faster machine learning through dynamic python bytecode transformation and graph compilation. In *Proceedings of the 29th ACM International Conference on Architectural Support for Programming Languages and Operating Systems, Volume 2*, ASPLOS '24, page 929–947, New York, NY, USA, 2024. Association for Computing Machinery. ISBN 9798400703850. doi: 10.1145/3620665.3640366. URL <https://doi.org/10.1145/3620665.3640366>.
  - [46] Tri Dao. Flashattention-2: Faster attention with better parallelism and work partitioning. In *The Twelfth International Conference on Learning Representations*, 2024. URL <https://openreview.net/forum?id=mZn2Xyh9Ec>.
  - [47] Yunjae Lee, Juntaek Lim, Jehyeon Bang, Eunyeong Cho, Huijong Jeong, Taesu Kim, Hyungjun Kim, Joonhyung Lee, Jinseop Im, Ranggi Hwang, Se Jung Kwon, Dongsoo Lee, and Minsoo Rhu. Debunking the cuda myth towards gpu-based ai systems, 2024. URL <https://arxiv.org/abs/2501.00210>.
  - [48] Intel. Intel gaudi 3 ai accelerator white paper, 2024. URL <https://cdrdv2-public.intel.com/817486/gaudi-3-ai>

- accelerator-white-paper.pdf. Accessed: 2025-01-31.
- [49] Meta. The llama 4 herd: The beginning of a new era of natively multimodal ai innovation, 2025. URL <https://ai.meta.com/blog/llama-4-multimodal-intelligence>.
  - [50] Intel. Intel gaudi 2 ai accelerator white paper, 2022. URL <https://cdrdv2-public.intel.com/784827/Gaudi2%20White%20Paper.pdf>. Accessed: 2025-01-31.
  - [51] Dan Zhao, Siddharth Samsi, Joseph McDonald, Baolin Li, David Bestor, Michael Jones, Devesh Tiwari, and Vijay Gadepally. Sustainable supercomputing for ai: Gpu power capping at hpc scale. In *Proceedings of the 2023 ACM Symposium on Cloud Computing*, pages 588–596, 2023.
  - [52] Jinqi Huang, Yi Xiong, Xuebing Yu, Wenjie Huang, Entong Li, Li Zeng, and Xin Chen. Slo-aware scheduling for large language model inferences. *arXiv preprint arXiv:2504.14966*, 2025.
  - [53] Ke Cheng, Zhi Wang, Wen Hu, Tiannuo Yang, Jianguo Li, and Sheng Zhang. Scoot: Slo-oriented performance tuning for llm inference engines. In *Proceedings of the ACM on Web Conference 2025*, pages 829–839, 2025.
  - [54] Minsu Kim, Seongmin Hong, RyeoWook Ko, Soongyu Choi, Hunjong Lee, Junsoo Kim, Joo-Young Kim, and Jongse Park. Oaken: Fast and efficient llm serving with online-offline hybrid kv cache quantization. In *Proceedings of the 52nd Annual International Symposium on Computer Architecture, ISCA '25*, page 482–497, New York, NY, USA, 2025. Association for Computing Machinery. ISBN 9798400712616. doi: 10.1145/3695053.3731019. URL <https://doi.org/10.1145/3695053.3731019>.
  - [55] June Yong Yang, Byeongwook Kim, Jeongin Bae, Beom-seok Kwon, Gunho Park, Eunho Yang, Se Jung Kwon, and Dongsoo Lee. No token left behind: Reliable kv cache compression via importance-aware mixed precision quantization, 2024. URL <https://arxiv.org/abs/2402.18096>.
  - [56] Abhinav Jangda, Jun Huang, Guodong Liu, Amir Hossein Nodehi Sabet, Saeed Maleki, Youshan Miao, Madanlal Musuvathi, Todd Mytkowicz, and Olli Saarikivi. Breaking the computation and communication abstraction barrier in distributed machine learning workloads. In *Proceedings of the 27th ACM International Conference on Architectural Support for Programming Languages and Operating Systems, ASPLOS '22*, page 402–416, New York, NY, USA, 2022. Association for Computing Machinery. ISBN 9781450392051. doi: 10.1145/3503222.3507778. URL <https://doi.org/10.1145/3503222.3507778>.
  - [57] AI @ Meta Llama Team. The llama 3 herd of models, 2024. URL <https://arxiv.org/abs/2407.21783>.
  - [58] Chenggang Zhao, Chengqi Deng, Chong Ruan, Damai Dai, Huazuo Gao, Jiashi Li, Liyue Zhang, Panpan Huang, Shangyan Zhou, Shirong Ma, Wenfeng Liang, Ying He, Yuqing Wang, Yuxuan Liu, and Y.X. Wei. Insights into deepseek-v3: Scaling challenges and reflections on hardware for ai architectures. In *Proceedings of the 52nd Annual International Symposium on Computer Architecture, ISCA '25*, page 1731–1745, New York, NY, USA, 2025. Association for Computing Machinery. ISBN 9798400712616. doi: 10.1145/3695053.3731412. URL <https://doi.org/10.1145/3695053.3731412>.
  - [59] Leo Gao, Jonathan Tow, Baber Abbasi, Stella Biderman, Sid Black, Anthony DiPofi, Charles Foster, Laurence Golding, Jeffrey Hsu, Alain Le Noac’h, Haonan Li, Kyle McDonell, Niklas Muennighoff, Chris Ociepa, Jason Phang, Laria Reynolds, Hailey Schoelkopf, Aviya Skowron, Lintang Sutawika, Eric Tang, Anish Thite, Ben Wang, Kevin Wang, and Andy Zou. A framework for few-shot language model evaluation, 07 2024. URL <https://zenodo.org/records/12608602>.

## APPENDIX

### A. Differences in hardware capabilities

We compare implementations of FP8 GEMM between NVIDIA GPUs and Intel Gaudi HPUs, identifying key differences despite both adhering to the FP8 specification [10].

**(Accumulation precision)** Hopper GPUs use a 14-bit accumulator for FP8 GEMMs [17], requiring casting to CUDA cores for higher precision. Software optimizations, such as applying FP32 accumulation to only one in four WGMMMA instructions, reduce error but increase kernel complexity and remain less precise than full FP32 accumulation. In contrast, Gaudi HPUs always accumulate in FP32 [11], ensuring higher numerical precision.

**(E4M3 range)** The Gaudi 2 follows the IEEE specification for special values, unlike NVIDIA GPUs, which use a single special value representation [30]. This results in seven fewer magnitude representations and a maximum value of 240 for E4M3 in the Gaudi 2 compared to 448 on NVIDIA GPUs. This has been addressed in the Gaudi 3, but we were unable to test these in our experiments.

**(Power-of-2 scaling)** Gaudi HPUs allow the modification of floating-point exponent biases to accelerate scaling factor application. The Gaudi 2 supports fixed hardware-accelerated scaling factors of  $2^{-8}, 2^{-4}, 2^0, 2^4$  for E4M3, while the Gaudi 3 extends this to arbitrary powers of 2 between  $2^{-32}$  and  $2^{31}$ . However, this feature is limited to GEMMs with per-tensor scaling factors.

**(Stochastic rounding)** During FP8 quantization, stochastic rounding can be applied when converting 16/32-bit floating-point values to FP8, similar to the technique proposed for FP32-to-BF16 conversion in [31]. This method is distinct from stochastic rounding applied at the inner-product [32].

**(Sparsity)** NVIDIA GPUs support semi-structured sparsity acceleration, potentially doubling tensor core peak throughput. However, despite attempts to leverage sparsity in LLMs [33, 34], dense GEMMs remain dominant due to accuracy loss and limited speedups. Gaudi HPUs do not support sparsity acceleration.

TABLE V

THROUGHPUT AND POWER MEASUREMENTS FOR SQUARE FP8 GEMMS WITH ROW-WISE SCALING. RATIOS OF MEASURED TFLOPS AND POWER TO THEIR PEAK VALUES ARE SHOWN IN PARENTHESES. H100 HAS PEAK FP8 THROUGHPUT OF 1989.9 TFLOPS WITH A TDP OF 700W, AND GAUDI 2 HAS 865 TFLOPS WITH A TDP OF 600W.

Device	(M,K,N)	TFLOPS	Power (W)	TFLOPS/W
Gaudi 2	1K	367.9 (42.5%)	375 (63%)	1.0
	2K	586.2 (67.8%)	460 (77%)	1.3
	4K	817.1 (94.5%)	460 (77%)	1.8
	8K	741.8 (85.8%)	490 (82%)	1.5
H100	1K	218.3 (11.0%)	350 (50%)	0.6
	2K	879.7 (44.2%)	690 (99%)	1.3
	4K	1167.6 (58.7%)	690 (99%)	1.7
	8K	1084.7 (54.5%)	690 (99%)	1.6

TABLE VI

GAUDI 2 THROUGHPUT IN TFLOPS FOR SCALED FP8 GEMM FOR SQUARE MATRICES OF THE GIVEN SIZE, EXCLUDING QUANTIZATION OVERHEAD. MEASURED THROUGHPUT RELATIVE TO THE PEAK FP8 THROUGHPUT (865 TFLOPS) IS INCLUDED IN PARENTHESES. HARDWARE ACCELERATION IS ONLY AVAILABLE FOR PER-TENSOR SCALING.

Type	Size	Per-Row	Per-Tensor	HW Accel.
E4M3	1K	494 (57.1%)	494 (57.1%)	494 (57.1%)
	2K	506 (58.5%)	641 (74.1%)	641 (74.2%)
	4K	735 (84.9%)	796 (92.1%)	801 (92.6%)
	8K	742 (85.7%)	822 (95.0%)	852 (98.4%)
E5M2	1K	306 (35.4%)	494 (57.1%)	493 (57.0%)
	2K	506 (58.5%)	642 (74.2%)	642 (74.2%)
	4K	735 (84.9%)	802 (92.7%)	802 (92.7%)
	8K	726 (83.9%)	825 (95.4%)	825 (95.4%)

TABLE VII  
H100 THROUGHPUT (TFLOPS) FOR SCALED FP8 GEMMS ON SQUARE MATRICES OF THE GIVEN SIZE, EXCLUDING QUANTIZATION OVERHEAD. RATIOS RELATIVE TO PEAK FP8 THROUGHPUT ARE SHOWN IN PARENTHESES. ONLY E4M3 RESULTS ARE REPORTED, AS PYTHON FUNCTIONS FOR E5M2 GEMM ARE UNAVAILABLE FOR GPUS.

Accum.	Size	Per-Row	Per-Tensor
FP32	1K	217 (11.0%)	186 (9.4%)
	2K	299 (15.1%)	840 (42.4%)
	4K	362 (18.3%)	1099 (55.5%)
	8K	396 (20.0%)	1300 (65.7%)
Fast	1K	237 (12.0%)	147 (7.4%)
	2K	810 (40.9%)	896 (45.3%)
	4K	1136 (57.4%)	1205 (60.9%)
	8K	1123 (56.8%)	1388 (70.1%)

### B. Stochastic rounding

Hardware-accelerated stochastic rounding for FP8 quantization is a unique feature of Gaudi HPUs, inspired by techniques such as those proposed in [31], and is not supported on NVIDIA GPUs. Equation 9 formalizes the concept, where a higher-precision value  $x$  is rounded up to  $x_{up}$  or down to  $x_{down}$  stochastically based on the distance from  $x$ .

$$x_{quantized} = \begin{cases} x_{up} & (p = \frac{x - x_{down}}{x_{up} - x_{down}}) \\ x_{down} & (p = \frac{x_{up} - x}{x_{up} - x_{down}}). \end{cases} \quad (9)$$

Stochastic rounding is expected to preserve more of the original numerical information post-quantization, potentially leading to improved model accuracy. However, empirical results in Table VIII indicate that stochastic rounding during quantization does not significantly enhance model accuracy. Furthermore, it may even lead to accuracy degradation in certain cases [31]. These findings suggest that while stochastic rounding during quantization theoretically retains more information, its practical benefits for FP8 inference in LLMs remain inconclusive.

TABLE VIII  
COMPARISON BETWEEN DIFFERENT FP8 DATA TYPES AND ROUNDING MODES FOR MMLU CoT 5-SHOT PERFORMANCE ON INSTRUCTION-TUNED LLAMA MODELS. STOCHASTIC ROUNDING PROVIDES LITTLE OR NO BENEFIT TO ACCURACY WHILE E5M2 IS DETRIMENTAL, ESPECIALLY FOR SMALLER MODELS. EXPERIMENTS WERE CONDUCTED ON A GAUDI 2 HPU.

Model	Data Type	Rounding	MMLU
Llama v3.2 1B Instruct	BF16	-	46.3%
	E4M3	SR	45.7%
	E4M3	RTN	45.5%
	E5M2	RTN	44.5%
Llama v3.2 3B Instruct	BF16	-	61.8%
	E4M3	SR	61.7%
	E4M3	RTN	61.6%
	E5M2	RTN	60.7%
Llama v3.1 8B Instruct	BF16	-	68.8%
	E4M3	SR	68.3%
	E4M3	RTN	68.3%
	E5M2	RTN	67.5%
Llama v3.3 70B Instruct	BF16	-	82.0%
	E4M3	SR	82.0%
	E4M3	RTN	82.0%
	E5M2	RTN	82.2%

### C. E4M3 vs. E5M2

Prior work has shown that E4M3 yields better accuracy than E5M2 on language tasks [29]. We extend this analysis to instruction-tuned models, as summarized in Table VIII. To identify the optimal format for inference, we compare the two using MMLU accuracy measured with LM Evaluation Harness (v0.4.7 [59]). Across all evaluated models, E4M3 consistently outperforms E5M2. Moreover, Table VI shows that GEMM throughputs for both formats are comparable, making E4M3 the preferred choice despite its smaller representational range on the Gaudi 2.